ADVANCED ENERGY MATERIALS

www.advenergymat.de

Novel Route to Fe-Based Cathode as an Efficient Bifunctional Catalysts for Rechargeable Zn–Air Battery

Sancan Han, Xiaoyi Hu, Jiacheng Wang, Xiaosheng Fang, and Yufang Zhu**

Efficient bifunctional oxygen reduction reaction (ORR) and oxygen evolution reaction (OER) catalysts are of great importance for rechargeable metal–air batteries. Herein, FeN_x/C catalysts are synthesized by pyrolysis of thiourea and agarose containing α-Fe_2O_3 nanoplate as Fe precursor, where α-Fe_2O_3 nanoplate can prevent the aggregation of carbon sheets to effectively improve the specific surface area during the carbonization process. The FeN_x/C-700-20 catalyst displays excellent catalytic performance for both ORR and OER activity in alkaline conditions with more positive onset potential (1.1 V vs the reversible hydrogen electrode) and half-wave potential, higher stability, and stronger methanol tolerance in alkaline solution, which are all superior to that of the commercial Pt/C catalyst. In this study, the detailed analyses demonstrate that the coexistence of Fe-based species and high content of Fe-N_x both play an important role for the catalytic activity. Furthermore, FeN_x/C-700-20 as cathode catalyst in Zn–air battery possesses higher charge–discharge stability and power density compared with that of commercial Pt/C catalyst, displaying great potential in practical implementation of for the rechargeable energy devices.

1. Introduction

With the rapid consumption of fossil fuels, there is an urgent demand for sustainable energy conversion and energy storage system.[1] In recent years, rechargeable metal–air batteries have been extensively studied and are considered as the most promising energy devices due to their high energy capacities, environment friendly.[2] Of particular interest, Zn–air batteries have attracted intensive study in terms of safety, low cost, and abundant resource.[3] Nevertheless, the rechargeable Zn–air batteries are still in the early period because of the sluggish kinetic for the oxygen reduction reaction (ORR) and oxygen evolution reaction (OER) during the charge and discharge process.[4] Hence, developing highly efficient catalysts as bifunctional electrodes for both OER and ORR are of great importance for the rechargeable Zn–air battery.

Noble-metal-based catalysts are considered as the effective electrocatalysts. Pt and Pt-based materials with controlled facets are traditionally known as the best active catalysts for ORR, but the formation of the oxide layer results in the limited OER activity, Ir and Ru-based materials are efficient for OER, but not active for ORR.[5] Therefore, much effort is made to develop more efficient, durable, and inexpensive bifunctional catalysts to replace precious-metal materials. Among them, metal oxide,[6] N-doped carbon materials and transition metal–N_x/C compounds have been extensively studied. However, metal oxides cline to undergo sintering and agglomeration, and N-doped carbon materials usually occurred two electron oxygen reduction reaction. In comparison, FeN_x/C catalyst with low cost, high activity, and stability has been emerging as the most promising bifunctional electrocatalyst.

Usually, the FeN_x/C catalysts are achieved by the pyrolysis of precursors containing iron source, nitrogen source, and carbon source. During the pyrolysis, nitrogen doped carbon materials and metal could offer more active site N-C and Fe-N_x. Furthermore, FeN_x/C catalysts with high specific surface area and mesopores could facilitate the transportation of ORR-relevant intermediates (H^+, OH^-, O_2), which can significantly improve the activity.[7] Several traditional methods in the literature were reported to synthesize the FeN_x/C catalysts. Zhong et al.[8] developed graphene-based nitrogen-doped porous carbon by the pyrolysis of zeolitic imidazolate framework (ZIF-8) on graphene oxide. However, the collapse of pores within carbon materials happens when metal–organic frameworks were acted as the porous precursors at the elevated temperature during the carbonization. Wan et al.[9] synthesized mesoporous N/S/Fe-C catalyst by in situ pyrolyzed in the presence of SiO_2 particles, but the additional complicated etching process are needed, resulting in the loss of active sites. Hence, it still remains great challenge

Dr. S. C. Han, X. Y. Hu, Prof. Y. F. Zhu
School of Materials Science and Engineering
University of Shanghai for Science and Technology
Shanghai 200093, P. R. China
E-mail: zjf2412@163.com
Dr. S. C. Han, Prof. Y. F. Zhu
Shanghai Innovation Institute for Materials
Shanghai 200444, P. R. China
Prof. J. C. Wang
State Key Laboratory of High Performance Ceramics and Superfine Microstructure
Shanghai Institute of Ceramics
Chinese Academy of Sciences
Shanghai 200050, P. R. China
Prof. X. S. Fang
Department of Materials Science
Fudan University
Shanghai 200433, P. R. China
E-mail: xshfang@fudan.edu.cn
The ORCID identification number(s) for the author(s) of this article can be found under https://doi.org/10.1002/aenm.201800955.

DOI: 10.1002/aenm.201800955

to develop effective approach for the highly efficient bifunctional FeN_x/C catalysts.

Driven by the above hints, in situ α-Fe_2O_3 nanoplate-template route was employed by pyrolysis of thiourea and agarose to fabricate the FeN_x/C catalysts with mesopores of ≈3.6 nm, where α-Fe_2O_3 nanoplates are used as the Fe precursor for the doping of FeN_x/C catalysts and the template to prevent the collapse of carbon sheets, in which urea acted as nitrogen source and agarose kept the effective separation of the Fe-based particles during the pyrolysis. The FeN_x/C catalysts with different pyrolysis temperature (600–900 °C) and ratios of precursor (α-Fe_2O_3 nanoplates: agarose: urea = 1:1:10, 1:1:15, 1:1:20, 1:1:25, 1:1:30) were synthesized to explore the appropriate composition and pyrolysis temperature, the resulting products were named as FeN_x/C-*a*-*b*, where *a* represents the calcined temperature and *b* denotes the mass ratio of [urea]/[α-Fe_2O_3], which are defined as FeN_x/C-600-20, FeN_x/C-700-20, FeN_x/C-800-20, FeN_x/C-900-20, FeN_x/C-700-10, FeN_x/C-700-15, FeN_x/C-700-20, FeN_x/C-700-25, and FeN_x/C-700-30, respectively. Among these catalysts, the FeN_x/C-700-20 shows the remarkable bifunctional ORR and OER activity under alkaline conditions, which are all superior to commercial Pt/C electrode. Notably, Zn–air battery with FeN_x/C-700-20 as the air electrode shows excellent rechargeable performance, displaying the higher power density and high cycling stability than that of commercial Pt/C catalyst. The work will provide a rational design for efficient bifunctional OER and ORR catalysts in rechargeable Zn–air battery.

2. Results and Discussion

The synthesis procedure for FeN_x/C catalysts is presented in **Scheme 1**. α-Fe_2O_3 nanoplates, agarose, and urea with different weight ratios are ground with a planetary mill for 2 h, followed by high-temperature pyrolysis from 600 to 900 °C. The temperature rised to 130 °C, urea was decomposed to NH_3 during the pyrolysis, which can react with agarose, producing NH_2-functionalized agarose.[10] With the increase of the temperature, NH_2-functionalized agarose was carbonized to produce the N-doped carbon sheets, meanwhile Fe-based nanocrystals would react with carbon atoms to produce carbide, and then carbide nanoparticles was embedded within graphitize carbon sheets, in which agarose keeps the effective separation for the particles during the pyrolysis.[10b] In order to further identify the composition changes under various treatment, X-ray diffraction patterns show that α-Fe_2O_3 were predominantly transformed to its carbide phase and FeO phase[11,12] (Figure S1, Supporting Information), which can be explained by the reduction reaction for α-Fe_2O_3 during the carbonization. In comparison, sample FeN_x/C-700-20 owns the most sharp diffraction intensity at 44.6°, implying more formation of Fe_3C phase.

The morphology and structure of the typical samples (FeN_x/C-700-20) were investigated by scanning electron microscopy (SEM) and transmission electron microscopy (TEM). As shown in **Figure 1**a,b, the morphology of the Fe phase changed significantly after the heat treatment, the α-Fe_2O_3 nanoplates were all transformed to the polydispersity of small Fe-phase nanoparticles on the carbon sheets, which can be ascribed to its carbide phase and FeO phase. These nanoparticles were coated by ultrathin graphitic layers and a well-defined crystalline lattice distance of ≈0.21 nm in Figure 1c corresponds to the d-spacing of (220) planes for Fe_3C or (110) crystallographic planes of cubic Fe.[13] The energy dispersive X-ray spectroscopy was carried out to further study the distributions of C, N, and Fe elements, as illustrated in Figure 1d. Uniformly distributed C and N throughout the selected area in the composites were observed, confirming high-level and uniform doping of N elements. While Fe signals are highly localized at the position where Fe nanoparticles exist. Obviously, the Fe signal partly overlaid with N signal at the atomic level, which roughly evidenced the dispersion of Fe-N_x sites in the FeN_x/C composites.

The Raman spectra of all the samples are shown in **Figure 2**. Two peaks observed at ≈1341 and ≈1580 cm^{-1}, which correspond to the disorder vibration mode of structural defects

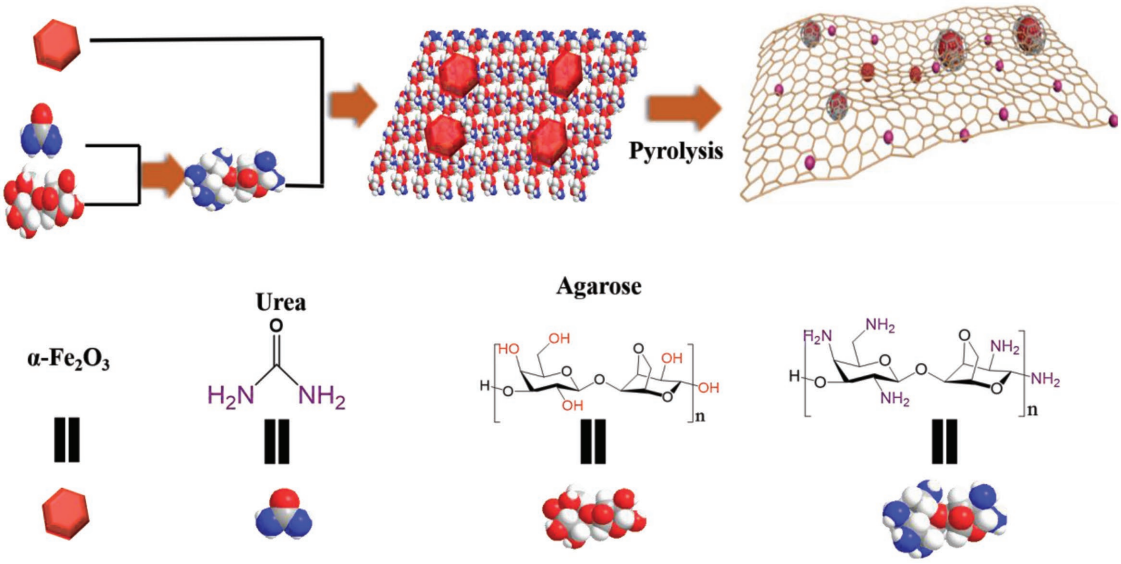

Scheme 1. The synthesis procedure for FeN_x/C catalysts.

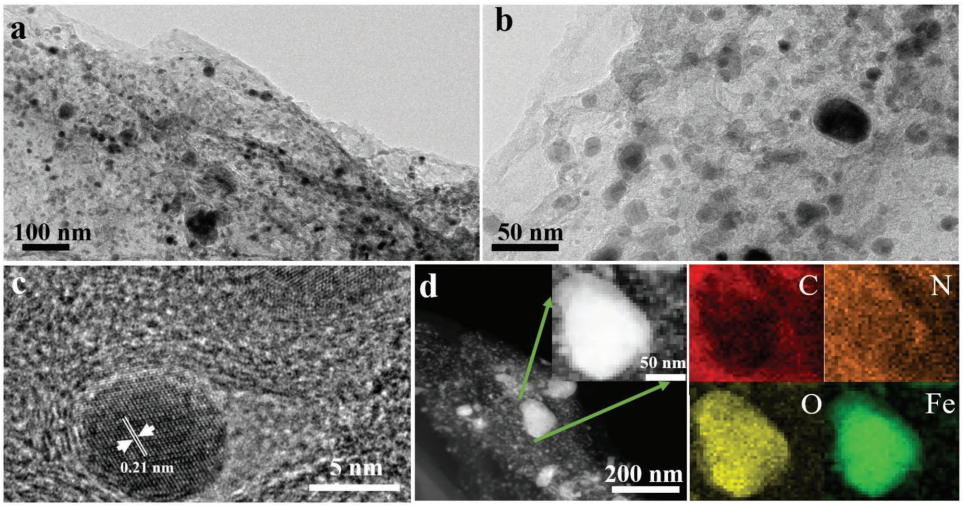

Figure 1. a,b) Representative TEM images of FeN_x/C-700-20. c) High-resolution TEM image. d) TEM mapping of the selected area (carbon, nitrogen, oxygen, and iron).

(D band) and well ordering scattering of graphitic carbon atoms (G band), respectively.[14] The I_D/I_G ratio could demonstrate the structural defect of the carbon sheets, higher I_D/I_G ratio means more N-doping on the carbon sheets. As can be seen, the I_D/I_G ratios for all the catalysts exhibit I_D/I_G of ≈1.0, which is all higher than that of the blank samples without N and Fe source (I_D/I_G ≈ 0.89) in Figure 2a, which indicates that the introduction of Fe and N could produce the structural defects in the graphic carbon sheets, resulting in the more formation of active site on the surface of the catalyst due to the Fe and N incorporation, which could be beneficial to the performance of ORR activity. Figure S2 in the Supporting Information showed the Brunauer–Emmett–Teller (BET) nitrogen physisorption isotherms, the curves for all the samples displayed a typical type IV isotherms with the average pore size of ≈3.6 nm (Figure S2b,d, Supporting Information). Figure S2e in the Supporting Information showed that the samples without α-Fe_2O_3 nanoplates displayed lower specific surface area compared with FeN_x/C-700-20, evidencing that the addition of α-Fe_2O_3 nanoplates could prevent the aggregation and collapse of the carbon sheets during the carbonization. The specific surface area and pore size for all the samples were summarized in Table S1 and S2 in the Supporting Information. As can be seen, the BET surface area decreases with the increase of the calcination temperature to 700 °C or higher, the mesoporous structure can be destroyed at the high temperature. Furthermore, more addition of urea could induce the enlargement of the surface area, which is possibly due to the activation of more nitrogen atoms.

The detailed elemental composition and the valence with different pyrolysis temperature and amount of the urea were analyzed by X-ray photoelectron spectroscopy (XPS). The N atom ratio for FeN_x/C-600-20, FeN_x/C-700-20, FeN_x/C-900-20, FeN_x/C-700-10, and FeN_x/C-700-30 were ≈18.57, ≈8.55, ≈5.27, ≈8.75, and ≈16.76, respectively, indicating the successful N doping in the catalysts. As can be seen in Figure S3a in the Supporting Information, more addition of urea could generate more N doping, meanwhile the amount of N doping in the catalysts decreases with the increase of the pyrolysis temperature. There exist two kind of nitrogen-doping species, which are N-doped carbon and N-doped Fe species. In Figure S3b–e in the Supporting Information and **Figure 3**b, high-resolution N1s spectra of the samples can be divided into four peaks, corresponding to Fe-N_x (≈400.0 eV), graphitic N (≈401.0 eV), pyridinic N

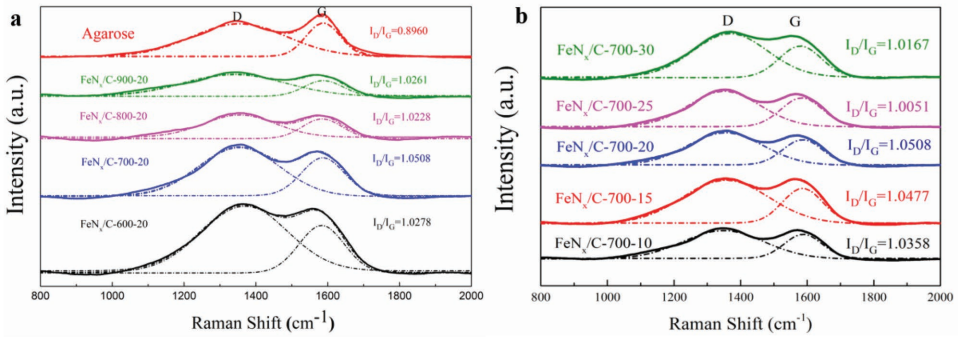

Figure 2. a) The Raman spectra for agarose (blank sample), FeN_x/C-600-20, FeN_x/C-700-20, FeN_x/C-800-20, and FeN_x/C-900-20. b) The Raman spectra for FeN_x/C-700-10, FeN_x/C-700-15, FeN_x/C-700-25, and FeN_x/C-700-30.

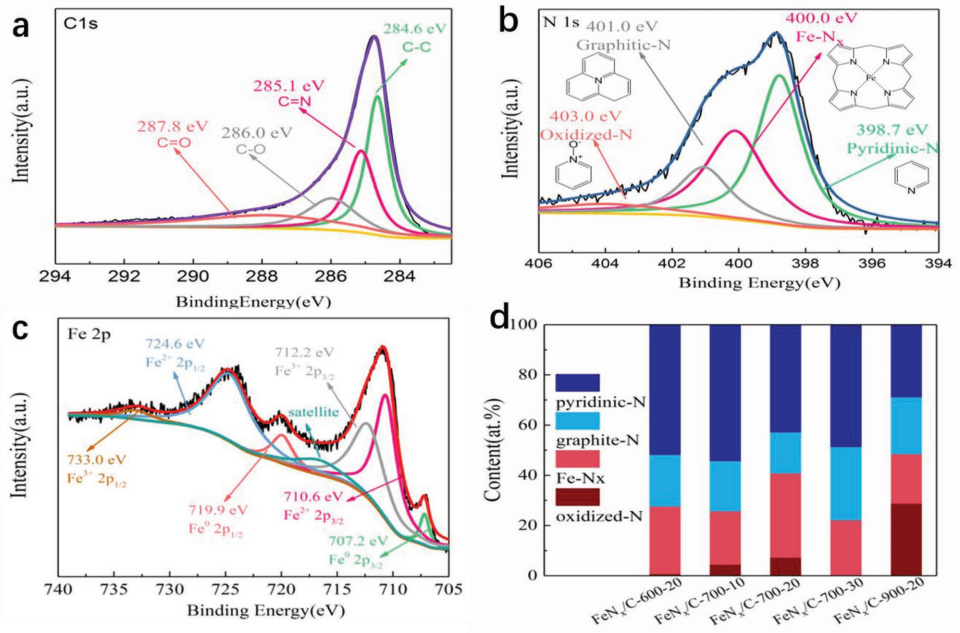

Figure 3. a) The Fe 2p XPS spectra of FeN_x/C-700-20. b) N 1s XPS spectra of FeN_x/C-700-20. c) The Fe 2p XPS spectra of FeN_x/C-700-20. d) Relative ratios of the deconvoluted peak areas of N 1s XPS spectra for FeN_x/C-600-20, FeN_x/C-700-20, FeN_x/C-900-20, FeN_x/C-700-10, and FeN_x/C-700-30.

(≈398.7 eV), and oxidized N (≈403.0 eV),[15–17] indicating the successful N-doping on Fe atoms. It has been reported that all N species except oxidized N are essential to ORR, and Fe-N_x composed by Fe atoms bonded with four nitrogen atoms is the main active site.[18] The calculated ratio of the deconvoluted peaks for N1s was shown in Figure 3d, FeN_x/C-700-20 owns the highest content of Fe-N_x among all the samples. Figure 3a shows the high-resolution C1s spectrum for FeN_x/C-700-20, a noticeable peak at ≈285.1 eV ascribed to C=N is clearly observed,[19,20] confirming the successful N-doping on the carbon sheets. The high-resolution Fe 2p spectrum for FeN_x/C-700-20 was analyzed to evidence the valence of Fe in Figure 3c. A weak peak at ≈719.9, and ≈707.2 eV ascribed to zero-valence metallic were observed, meanwhile the main peaks at ≈724.6, and ≈710.6 eV were assigned to Fe $2p_{1/2}$ and Fe $2p_{3/2}$ of Fe(II) ions,[21,22] respectively, indicating that the use of α-Fe_2O_3 nanoplate as the iron precursor could achieve relatively high content of Fe^{2+} in the catalyst. As previous work reported, abundant Fe^{2+} species could be beneficial to form the active center of Fe^{2+}-N_{2+2} and Fe^{2+}-N_4 in superior ORR activity,[23] which is consistent with above peak split of N1s spectrum.

Cyclic voltammetry (CV) and linear sweep voltammetry (LSV) curves for all the samples and Pt/C on a rotating disk electrode in O_2-saturated 0.1 M aqueous KOH are measured to investigate the ORR performance, as shown in Figures S4–S7 in the Supporting Information and **Figure 4**a,b. The electrode potential based on the reversible hydrogen electrode (RHE) potential was converted from the Hg/HgO electrode: $E_{RHE} = E_{SCE} + 0.0591 \times pH + E^*_{SCE}$. In Figures S4 and S5 in the Supporting Information, FeN_x/C-600-20, FeN_x/C-900-20, FeN_x/C-700-10, FeN_x/C-700-15, and FeN_x/C-700-30 did not exhibit redox peak in CV curves; however, FeN_x/C-700-20, FeN_x/C-800-20, and FeN_x/C-700-25 show a well-defined cathodic oxygen reduction peak, indicating the importance of the ratio of precursors and the pyrolysis temperature. Among various parameters, diffusion-limiting current, the half-wave potential and onset potential are important to evaluate the ORR activity, which were shown in Figure 4c,d. In comparison, the onset potential and half-wave potential for FeN_x/C-700-20 catalysts was ≈1.1 and ≈0.9 V, which is ≈100 mV higher than that of commercial 20% Pt/C catalyst. As summarized in Table S3 in the Supporting Information, the present FeN_x/C-700-20 electrode in this work owns the most positive half-wave potential and onset potential, indicating the best ORR activity compared with that of previous reports. The excellent ORR activity of FeN_x/C-700-20 catalysts is further evidenced by the smallest Tafel slope of 93 mV dec^{-1}, which is very close to that of commercial 20% Pt/C catalyst (84 mV dec^{-1}), as shown in **Figure 5**a,b. The above results are in agreement with XPS results that FeN_x/C-700-20 owns the highest content of reactive site Fe-N_x, which is the main active center for ORR.

The typical current-potential curves for all the samples during the ORR process at various rotating rates, as shown in Figures S6 and S7 in the Supporting Information. The current density increases with the increasing of rotation rate, which can be explained by the shortened diffusion layer at high speed. Figure 5c displayed the corresponding Koutecky–Levich (K–L) plots, good linearity with parallelism from ≈0.2 to ≈0.5 V was clearly observed, indicating the first-order kinetics in FeN_x/C-700-20 catalysts. According to the K–L equation, the electron transfer numbers for FeN_x/C-700-20 and commercial Pt/C were calculated to be ≈3.95 and ≈4.0, respectively, indicating that ORR in FeN_x/C-700-20 and Pt/C catalysts dominantly proceeds with efficient four-electron transfer pathway. Figure 5d show the CV curves of FeN_x/C-700-20 electrode in 0.1 M N_2- and O_2-saturated aqueous KOH. Only featureless double-layer charge current happened in N_2-saturated electrolyte, whereas a well-defined reduction peak at ≈0.86 V in

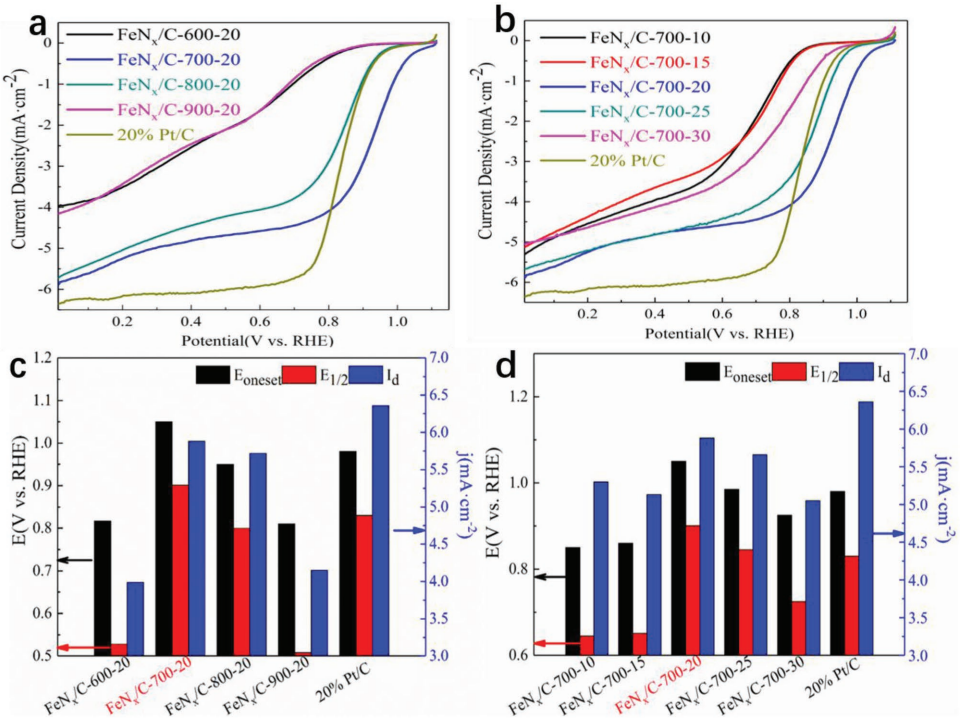

Figure 4. a,b) LSV curves for FeN_x/C-600-20, FeN_x/C-700-20, FeN_x/C-800-20, FeN_x/C-900-20, FeN_x/C-700-10, FeN_x/C-700-15, FeN_x/C-700-20, FeN_x/C-700-25, FeN_x/C-700-30, and commercial 20% Pt/C catalysts at a rotating speed of 1600 rpm and c,d) diffusion-limiting current, the half-wave potential and onset potential of all the samples.

O_2-saturated aqueous 0.1 M KOH can be observed, suggesting the pronounced electrocatalytic ORR activity. The OER performance of FeN_x/C-700-20 and 20% Pt/C catalyst was evaluated by LSV curves at 1600 rpm in 0.1 M KOH. As shown in Figure 5e, the FeN_x/C-700-20 exhibited higher current density and lower onset potential than that of commercial 20% Pt/C catalyst. Compared with IrO_2, FeN_x/C-700-20 also displayed lower onset potential, though lower current density was observed over a large potential range above the onset potential. In comparison, FeN_x/C-700-20 electrocatalysts displayed smaller Tafel slope (219 mV dec^{-1}) than that of 20% Pt/C catalyst (276 mV dec^{-1}) in Figure 5f, which indicate its excellent kinetic reaction for OER activity.

The LSV curves for the sample with or without α-Fe_2O_3 as the precursor and the FeN_x/C-700-20 samples using acid treatment were shown in Figure S8a,b in the Supporting Information. In Figure S8a in the Supporting Information, the catalyst without α-Fe_2O_3 as the precursor showed a significant decrease in the diffusion-limiting current and the negative shift of the onset potential, which indicated the importance of Fe source, evidencing that the high ORR activity possibly mainly from Fe-N_x or Fe-based species.[24–27] As shown in Figure S8b in the Supporting Information, a degree of decrease for ORR was also observed in FeN_x/C-700-20 electrode using acid treatment to remove the Fe-based particles, indicating that Fe-based particles also played an important role in high ORR activity. The results above suggest the coexistence of Fe-based particles and Fe-N_x are both necessary in improving ORR activity for the FeN_x/C-700-20 electrode. For OER reaction process, positively charged carbon and Fe around nitrogen could easily adsorb OH^-, and the transfer of two O_{ads} such as O_2^{2-} and O^{2-}, also become easily, which result in the improved OER activity.[28]

The rotating ring-disk electrode (RRDE) voltammograms at 1600 rpm in 0.1 M aqueous KOH were carried out to determine the H_2O_2 percent yield (%) and the electron transfer number (n) to further evidence the superior ORR activity for FeN_x/C-700-20, which can be calculated from the disk current and the ring current.[29,30] As shown in **Figure 6**b, the H_2O_2 percent yield was less than ≈5%, which is slightly higher than that of commercial Pt/C. The electron transfer number is almost constant at ≈4.00 range from ≈0.6 to ≈1.0 V, and then gradually decreases to ≈3.9, which is consistent with the value of n based on the K–L plots, further evidencing the four electron pathway for FeN_x/C-700-20. The durability of FeN_x/C-700-20 with respect to commercial Pt-C catalysts was compared by chronoamperometric measurements at −0.6 V at 1600 rpm. As revealed in **Figure 7**a, high current retention (≈90%) compared with the original value after 20 000 s, in contrast, the commercial Pt/C showed a rapid decrease with ≈70% retention. The introduction of methanol would result in a significantly decrease of the commercial Pt/C catalyst, whereas no noticeable change happened for FeN_x/C-700-20 electrode, suggesting a great tolerance to methanol, as shown in Figure 7b. These results confirm excellent stability of FeN_x/C-700-20 catalyst, which can be possibly explained by that the Fe-based particles within the carbon sheets could prevent the aggregation of the final products, keeping continuous electron transfer pathways between the carbon sheets, which is consistent with the BET results above.

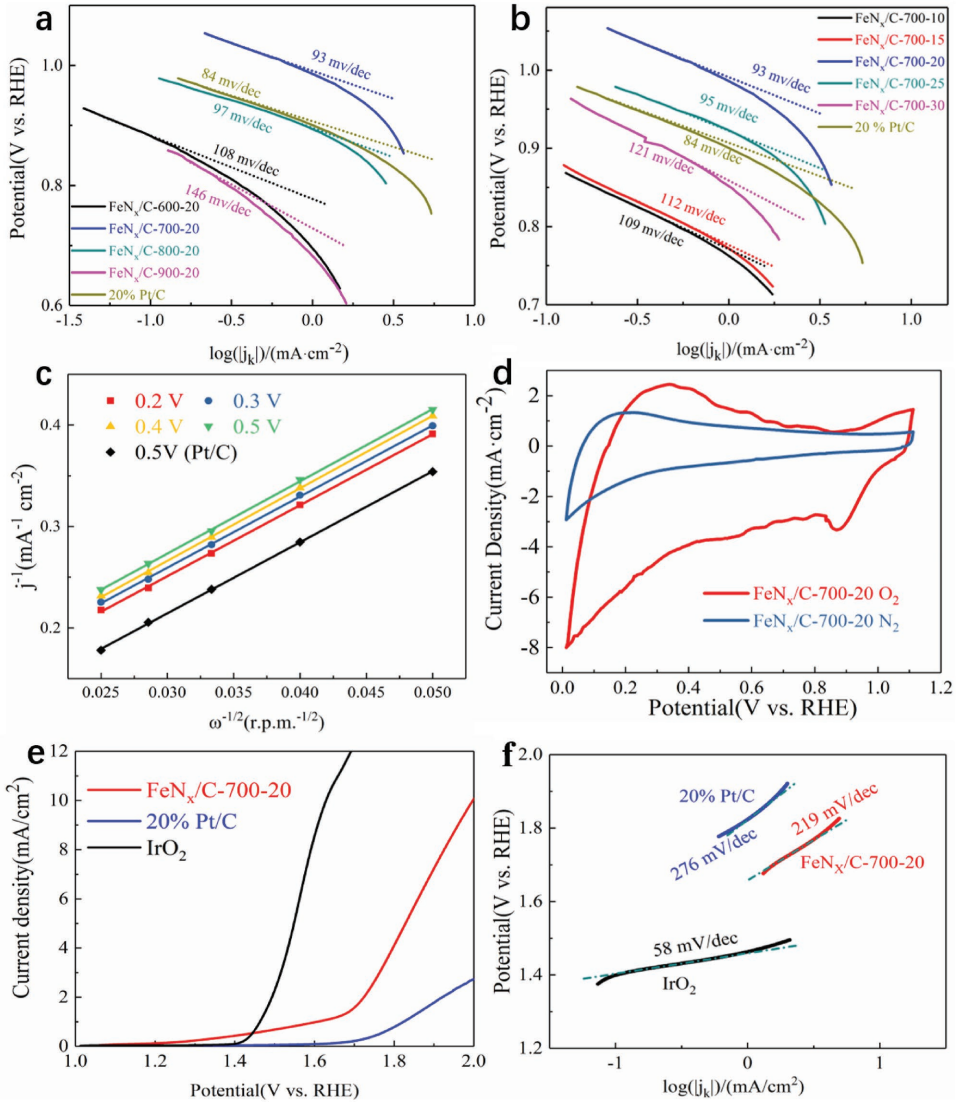

Figure 5. a,b) Tafel slopes of all the samples and Pt/C catalysts, c) corresponding K–L plots at various potentials for FeN_x/C-700-20 and commercial 20% Pt/C catalysts, d) CVs of FeN_x/C-700 in O_2- and N_2-saturated 0.1 M aqueous KOH, and e,f) OER curves and tafel slopes of FeN_x/C-700-20, commercial 20% Pt/C, and IrO_2 catalysts in 0.1 M aqueous KOH.

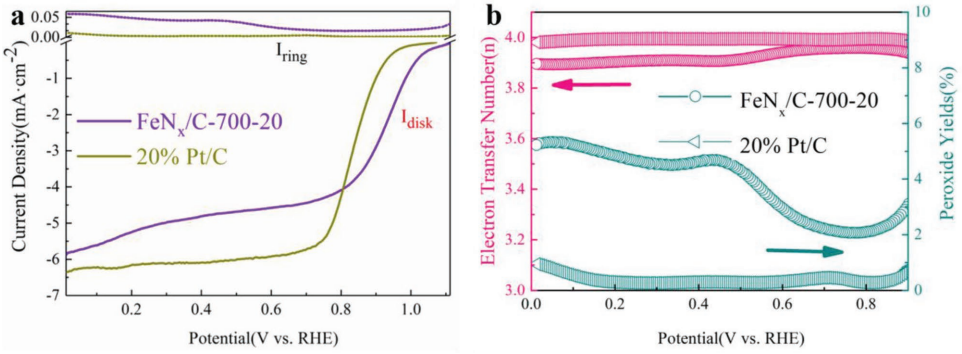

Figure 6. a) RRDE voltammograms of the ORR on FeN_x/C-700-20 and commercial 20% Pt/C electrode in an O_2-saturated 0.1 M aqueous KOH at 1600 rpm. b) Electron transfer number and peroxide yields of FeN_x/C-700-20 and commercial 20% Pt/C electrode at the rotation speed of 1600 rpm.

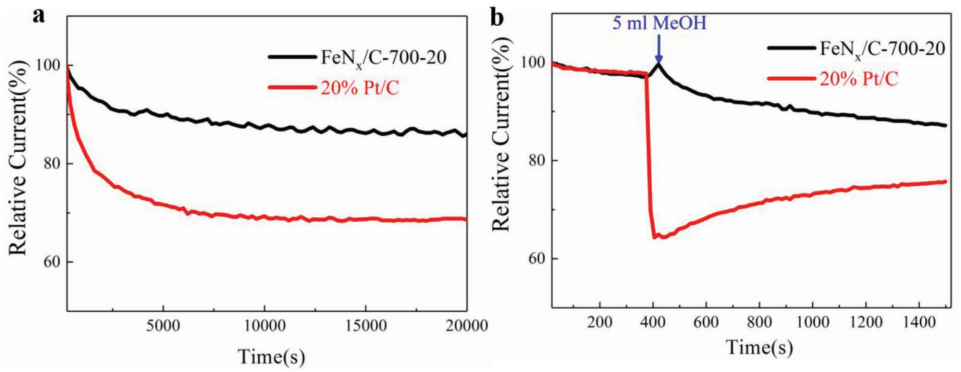

Figure 7. a) Chronoamperometric response of FeN_x/C-700-20 and commercial 20% Pt/C at –0.6 V in O_2-saturated 0.1 M KOH solution (1600 rpm). b) Chronoamperometric responses of FeN_x/C-700-20 and commercial 20% Pt/C at –0.6 V in O_2-saturated 0.1 M KOH solution (1600 rpm) followed by 1.0 M methanol.

As shown in **Figure 8**a, a home-made rechargeable Zn–air battery was constructed, FeN_x/C-700-20 as the air electrode and 6.0 M KOH as the electrolyte. Figure 8b displayed the charge and discharge polarization curves for the Zn–air battery. As can be seen, the open circuit voltage for FeN_x/C-700-20-based Zn–air battery is ≈1.6 V, lower charge potential and higher discharge platform were obtained at high current density than that of the Pt/C electrode, and the high voltage loss for the Pt/C-based Zn–air battery was observed with the increase of the current density, which showed that FeN_x/C-700-20-based Zn–air battery owned much enhanced voltaic efficiency. The power density and discharge polarization curves were displayed in Figure 8c, the Pt/C catalysts shows the peak power density of ≈27 mW cm^{-2} at the current density of 55 mA cm^{-2}; however, the power density for FeN_x/C-700-20 can be achieved to ≈36 mW cm^{-2} at the current density of 80 mA cm^{-2}, outperforming Pt/C electrode in this work. The long-term cycle stability is one of the most important factors for Zn–air batteries, the experiment with short internal is an effective toll to examine the rechargeable ability for the air electrode. The charge and discharge cycling tests were performed at constant current density of 5 mA cm^{-2} with per cycle of 10 min. The voltage profiles for FeN_x/C-700-20- and Pt/C-based rechargeable Zn–air batteries are shown in Figure 8d,e. In comparison with Pt/C-based Zn–air batteries, the steady and low voltage gap was observed for FeN_x/C-700-20-based battery, indicating better rechargeability for FeN_x/C-700-20-based battery. The results above show that the FeN_x/C-700-20 catalysts own excellent ORR/OER activity and stability in rechargeable Zn–air batteries.

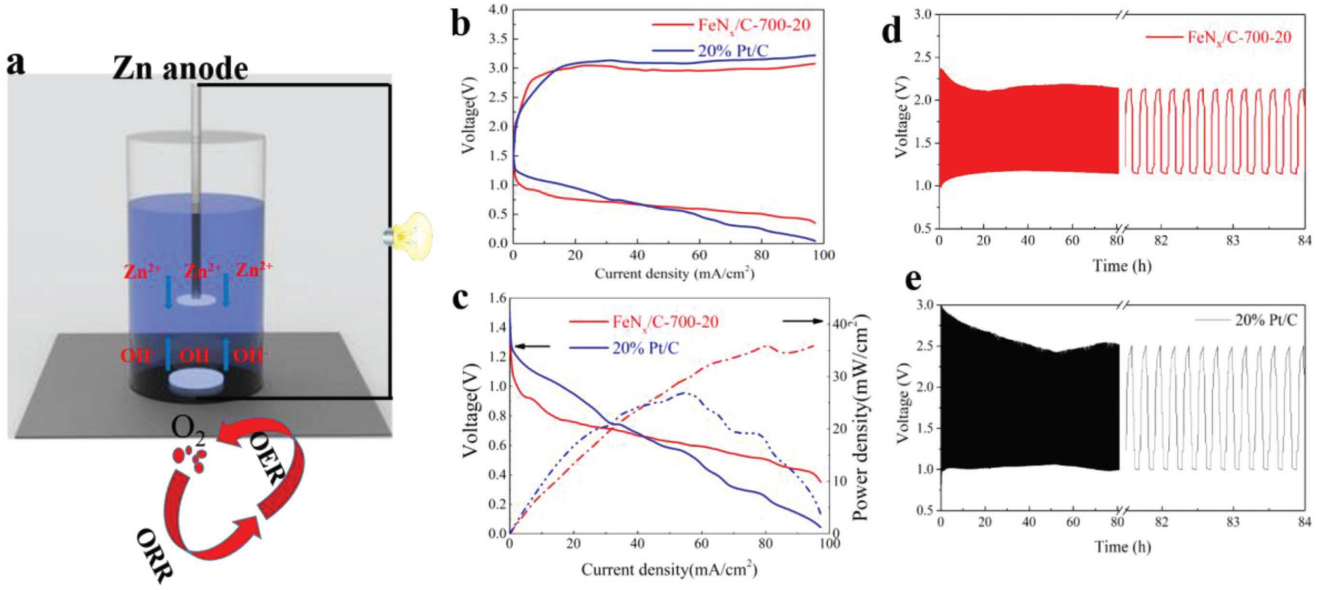

Figure 8. a) Schematic representation of the rechargeable Zn–air battery. b) Charge and discharge polarization curves for the Zn–air batteries at different current density and c) discharge and power density curves for the Zn–air batteries with FeN_x/C-700-20 and 20% Pt/C catalysts at different current density. Galvanostatic charge–discharge cycling curves at 5 mA cm^{-2} of rechargeable Zn–air batteries with d) FeN_x/C-700-20 and e) commercial 20% Pt/C as catalysts with a duration of 10 min per cycle.

3. Conclusions

In summary, bifunctional FeN_x/C catalysts were successfully synthesized by a simple pyrolysis procedure with different temperature and ratio of precursors, wherein α-Fe_2O_3 nanoplates were used as the Fe precursor and the template to prevent the aggregation of the carbon sheets, and agarose keeps the effective separation for the Fe-based particles during the pyrolysis. Among all these samples, FeN_x/C-700-20 catalysts showed more superior ORR and OER activity, durability, and great tolerance for methanol in alkaline media. Especially, the FeN_x/C-700-20 catalysts can be successfully employed as Zn–air batteries, displaying the higher power density and excellent charge-discharging stability than that of Pt/C electrode. The work provides a new method to construct effective bifunctional electrocatalysts for reversible energy devices.

4. Experimental Section

Synthesis of α-Fe_2O_3: The α-Fe_2O_3 was prepared by a one-step hydrothermal method according to a published procedure.[31] First, 1.352 g $FeCl_3 \cdot 6H_2O$ (Sinopharm Chemical Reagent Corp., ≥99%) was added to ethanol with a trace addition of deionized water (3.5 mL) under vigorous stirring for 30 min, 4 g sodium acetate (Sinopharm Chemical Reagent Corp., ≥99%) was added to the mixture solution for another 1 h stirring. Then the mixture was transferred to a Teflon-lined autoclave (100 mL) and followed by hydrothermal treatment at 180 °C for 24 h. Following natural cooling to ambient temperature, the samples were collected by centrifugation and washed with deionized water and ethanol three times, respectively. The obtained products were dried in the oven at 60 °C for 6 h for characterization.

Synthesis of FeN_x/C Catalysts: In a typical experiment, α-Fe_2O_3 nanoplates (50 mg), agarose (50 mg), and urea (the mass ratio of [α-Fe_2O_3]/[urea] ranged from 1:10 to 1:30) were physically ground about 20 min. The mixture was transferred into a quartz boat and ventilated 0.5 h with Ar in the box furnace for the elimination of air. After that, the mixture was calcined 1 h at a high temperature in the range of 600–900 °C with a rate of 10 °C min^{-1}. The resulting products were named as FeN_x/C-*a*-*b*, where *a* represents the calcined temperature and *b* denotes the mass ratio of [urea]/[α-Fe_2O_3].

Characterization: The wide-angle X-ray diffraction patterns were gained on a D8 ADVANCE powder diffractometer using Cu Kα radiation (λ = 0.15405 Å). The morphology was observed by SEM and TEM using field electron and ion company (FEI) Quanta 450 field emission scanning electron microscope and Tecnai G2 F30 transmission electron microscope with an acceleration voltage of 300 kV, respectively. Raman spectra were collected by using Raman Microscopy (Horiba, LabRAM HR Evolution, France) with an excitation wavenumber of 532 nm. Nitrogen adsorption–desorption isotherms were acquired on a Micromeritics TristarII3020 surface area and pore size analyzer. The surface area, pore size, and pore volume were determined by BET and Barrett–Joyner–Halenda methods. XPS was tested with an ESCALAB 250 X-ray photoelectron spectrometer using Al K_α (h_v = 1486.6 eV) radiation.

Electrochemical Test: All the electrochemical tests were conducted in a three-electrode system with an electrochemical workstation (Pine Instrument Co.). The catalyst inks were prepared by ultrasonically dispersing 5 mg of the catalyst in a mixed solution contained 500 µL of deionized water, 500 µL of ethanol, and 30 µL of Nafion (5 wt%) solution. Then, 20 µL of ink was dropped into the working electrode (glassy carbon electrode) and dried at 50 °C. The amount of catalyst loading is 0.5 mg cm^{-2} for all the samples. The Pt foil and saturated calomel electrode (SCE) were employed as the counter electrode and the reference electrode, respectively. And the electrolyte was 0.1 M KOH solution. According to the following equation, the potentials versus the SCE were converted to the RHE scale[32,33]

$$E_{RHE} = E_{SCE} + 0.0591 \times pH + E^*_{SCE} \quad (1)$$

The electrolyte was purged with high-purity O_2 or N_2 for 30 min before testing. For the ORR performance, the CV curves were collected at the rate of 100 mV s^{-1} with the potential from 1.2 to 0.1 V versus the RHE, the LSV curves were conducted from 1.2 to 0.1 V versus the RHE, with a scan rate of 10 mV s^{-1} at different rotation rates of 400–2025 rpm.

The electron transfer number (*n*) was calculated by the K–L Equations (2) and (3) as follows[34,35]

$$\frac{1}{j} = \frac{1}{j_k} + \frac{1}{B\omega^{1/2}} \quad (2)$$

$$B = 0.2nFC_{O_2}D_{O_2}^{2/3}\upsilon^{-1/6} \quad (3)$$

where j is the measured current density, j_k is the kinetic current density, ω is the electrode rotation rate, n is the electron transfer number, F is the Faraday constant (96 485 C mol^{-1}), Co_2 is the bulk concentration of O_2 (1.2×10^{-3} mol L^{-1} for 0.1 M KOH solution), Do_2 is the diffusion coefficient of O_2 (1.9×10^{-5} cm^2 s^{-1} for 0.1 M KOH solution), and υ is the kinetic viscosity (0.01 cm^2 s^{-1} for 0.1 M KOH solution). The constant 0.2 is employed if the rotation rate is expressed in rpm.

The RRDE was adopted for the measurement of the peroxide (H_2O_2) yields (%) and the electron transfer number (*n*) during the ORR process, which can be calculated by Equation (4) and (5)[36,37]

$$H_2O_2(\%) = 200\frac{I_r/N}{I_d + I_r/N} \quad (4)$$

$$n = 4\frac{I_d}{I_d + I_r/N} \quad (5)$$

where I_r is the ring current, I_d is the disk current, and the N is a constant of 0.37, representing the ring collection efficiency of the electrode.

Zn–Air Battery Test: The rechargeable Zn–air battery experiments were carried out with home-made Zn–air battery, as shown in Figure 8a. The cathode was prepared by pressing FeN_x/C-700-20 catalysts, carbon black, and polyvinylidene fluoride (weight ratio of 7:2:1) on a nickel foam at 10 MPa and dried at 60 °C for 2 h (≈2.0 mg cm^{-2}). The zinc plate was used as the air electrodes. Both electrodes were assembled into a home-made Zn–air battery with 6 M KOH aqueous solution being used as the electrolyte. The cycling was carried out for 10 min cycles (5 min discharge and 5 min charge) and a current density of 5 mA cm^{-2}.

Supporting Information

Supporting Information is available from the Wiley Online Library or from the author.

Acknowledgements

The work was supported by the Shanghai Sailing Program (17YF1412700), National Natural Science Foundation of China (Grant Nos. 51572172, 11674061, and 51471051), Young Teachers in Shanghai Colleges and Universities (ZZslg16062), and Cultivation fund of University of Shanghai for Science and Technology (ZR18PY06).

Conflict of Interest

The authors declare no conflict of interest.

Keywords

bifunctional air electrodes, charge–discharge stability, oxygen evolution reaction, oxygen reduction reaction, Zn–air batteries

Received: March 26, 2018
Revised: April 16, 2018
Published online: May 21, 2018

[1] a) J. Fu, Z. P. Cano, M. G. Park, A. Yu, M. Fowler, Z. Chen, *Adv. Mater.* **2017**, *29*, 1604685; b) C. Breyer, A. Gerlach, *Prog. Photovoltaics* **2013**, *21*, 121; c) L. Peng, L. F. Hu, X. S. Fang, *Adv. Funct. Mater.* **2014**, *24*, 2591.

[2] a) Y. Li, H. Dai, *Chem. Soc. Rev.* **2014**, *43*, 5257; b) X. Chen, B. Liu, C. Zhong, Z. Liu, J. Liu, L. Ma, Y. Deng, X. Han, T. Wu, W. Hu, *Adv. Energy Mater.* **2017**, *7*, 1700779; c) C. Guan, A. Sumboja, H. Wu, W. Ren, X. Liu, H. Zhang, Z. Liu, C. Cheng, S. J. Pennycook, J. Wang, *Adv. Mater.* **2017**, *29*, 1704117; d) M. Yu, Z. Wang, C. Hou, Z. Wang, C. Liang, C. Zhao, Y. Tong, X. Lu, S. Yang, *Adv. Mater.* **2017**, *29*, 1602868; e) M. Yang, X. Hu, Z. Fang, L. Sun, Z. Yuan, S. Wang, W. Hong, X. Chen, D. Yu, *Adv. Funct. Mater.* **2017**, *27*, 1701971; f) J. S. Lee, T. K. Sun, R. Cao, N. S. Choi, M. Liu, K. T. Lee, J. Cho, *Adv. Energy Mater.* **2011**, *1*, 34; g) R. Cao, J. S. Lee, M. Liu, J. Cho, *Adv. Energy Mater.* **2012**, *2*, 816.

[3] a) C. Y. Su, H. Cheng, W. Li, Z. Q. Liu, N. Li, Z. Hou, F. Q. Bai, H. X. Zhang, T. Y. Ma, *Adv. Energy Mater.* **2017**, *7*, 1602420; b) F. Meng, H. Zhong, J. Yan, X. Zhang, *Nano Res.* **2017**, *10*, 4436.; c) C. Tang, B. Wang, H. F. Wang, Q. Zhang, *Adv. Mater.* **2017**, *29*, 1703185; d) C. Tang, H. F. Wang, X. Chen, B. Q. Li, T. Z. Hou, B. S. Zhang, Q. Zhang, M. M. Titirici, F. Wei, *Adv. Mater.* **2016**, *28*, 6845.

[4] a) H. Li, Z. Guo, X. Wang, *J. Mater. Chem. A* **2017**, *5*, 21353; b) C. Wu, Y. Zhang, D. Dong, H. Xie, J. Li, *Nanoscale* **2017**, *9*, 12432; c) Y. Tang, F. Jing, Z. Xu, F. Zhang, Y. Mai, D. Wu, *ACS Appl. Mater. Inter.* **2017**, *9*, 12340; d) X. X. Ma, X. H. Dai, X. He, *ACS Sustainable Chem. Eng.* **2017**, *5*, 9848.

[5] a) Y. Luo, N. Alonso-Vante, *Electrochim. Acta* **2015**, *179*, 108; b) D. W. Banham, J. N. Soderberg, V. I. Birss, *J. Phys. Chem. C* **2009**, *113*, 10103; c) W. S. Song, L. Lian, X. Wang, H. Sun, *Appl. Mech. Mater.* **2014**, *672*, 657; d) P. Yuan, R. J. Nielsen, W. A. Goddard, *J. Am. Chem. Soc.* **2017**, *139*, 149; e) D. Y. Kuo, J. K. Kawasaki, J. N. Nelson, J. Kloppenburg, G. Hautier, K. M. Shen, D. G. Schlom, S. Jin, *J. Am. Chem. Soc.* **2017**, *139*, 3473.

[6] a) H. C. Chang, S. Y. Lee, S. H. Park, S. I. Woo, *Appl. Catal., B* **2011**, *103*, 362; b) Y. Liang, H. Wang, J. Zhou, Y. Li, J. Wang, T. Regier, H. Dai, *J. Am. Chem. Soc.* **2012**, *134*, 3517.

[7] W. Niu, L. Li, X. Liu, N. Wang, J. Liu, W. Zhou, Z. Tang, S. Chen, *J. Am. Chem. Soc.* **2015**, *137*, 5555.

[8] H. X. Zhong, J. Wang, Y. W. Zhang, W. L. Xu, W. Xing, D. Xu, Y. F. Zhang, X. B. Zhang, *Angew. Chem.* **2014**, *53*, 14235.

[9] I. Kone, X. Ao, T. Yang, C. Yu, L. Jia, Y. Chen, Y. Sun, J. Y. Xiao, P. Wan, *ACS Appl. Mater. Inter.* **2017**, *9*, 20963.

[10] a) R. Wang, J. Li, S. Cai, Y. Zeng, H. Zhang, H. Cai, D. H. Tang, *Chempluschem* **2016**, *81*, 1; b) C. Schliehe, J. Yuan, S. Glatzel, K. Siemensmeyer, K. Kiefer, C. Giordano, *Cheminformatics* **2012**, *43*, 2716.

[11] Z. Wen, S. Ci, F. Zhang, X. Feng, S. Cui, S. Mao, S. Luo, Z. He, J. Chen, *Adv. Mater.* **2012**, *24*, 1398.

[12] V. Armel, S. Hindocha, F. Salles, S. Bennett, D. Jones, F. Jaouen, *J. Am. Chem. Soc.* **2017**, *139*, 453.

[13] W. J. Jiang, L. Gu, L. Li, Y. Zhang, X. Zhang, L. Zhang, J. Wang, J. S. Hu, Z. Wei, L. J. Wan, *J. Am. Chem. Soc.* **2016**, *138*, 3570.

[14] L. W. Zhang, H. B. Fu, Y. F. Zhu, *Adv. Funct. Mater.* **2010**, *18*, 2180.

[15] H. Ren, Y. Wang, Y. Yang, X. Tang, Y. Peng, H. Peng, L. Xiao, J. Lu, H. D. Abruña, L. Zhuang, *ACS Catal.* **2017**, *7*, 6485.

[16] W. Liu, L. Zhang, X. Liu, X. Liu, X. Yang, S. Miao, W. Wang, A. Wang, T. Zhang, *J. Am. Chem. Soc.* **2017**, *139*, 10790.

[17] L. Lin, Q. Zhu, A.-W. Xu, *J. Am. Chem. Soc.* **2014**, *136*, 11027.

[18] N. Ramaswamy, U. Tylus, Q. Jia, S. Mukerjee, *J. Am. Chem. Soc.* **2013**, *135*, 15443.

[19] J. Li, Q. Jia, S. Ghoshal, W. Liang, S. Mukerjee, *Langmuir* **2017**, *33*, 9246.

[20] Y. Ye, H. Li, F. Cai, C. Yan, R. Si, S. Miao, Y. Li, G. Wang, X. Bao, *ACS Catal.* **2017**, *7*, 7638.

[21] Z. Y. Wu, X. X. Xu, B. C. Hu, H. W. Liang, Y. Lin, L. F. Chen, S. H. Yu, *Angew. Chem.* **2015**, *54*, 8179.

[22] Z. Zhang, M. Dou, H. Liu, L. Dai, F. Wang, *Small* **2016**, *12*, 4193.

[23] U. I. Koslowski, I. A. Wurmbach, S. Fiechter, P. Bogdanoff, *J. Phys. Chem. C* **2008**, *112*, 15356.

[24] a) G. A. Ferrero, K. Preuss, A. Marinovic, A. B. Jorge, N. Mansor, D. J. Brett, A. B. Fuertes, M. Sevilla, M. M. Titirici, *ACS Nano* **2016**, *10*, 5922; b) Y. W. Ju, S. Y. Yoo, C. M. Kim, S. Kim, I. Y. Jeon, J. Shin, J. B. Baek, G. Kim, *Adv. Sci.* **2016**, *3*, 1500205. c) C. Y. Su, H. Cheng, W. Li, Z. Q. Liu, N. Li, Z. F. Hou, F. Q. Bai, H. X. Zhang, T. Y. Ma, *Adv. Energy Mater.* **2017**, *7*, 1602420.

[25] a) W. He, C. Jiang, J. Wang, L. Lu, *Angew. Chem.* **2014**, *53*, 9503; b) H. Cheng, M. L. Li, C. Y. Su, N. Li, Z. Q. Liu, *Adv. Funct. Mater.* **2017**, *27*, 1701833. c) Y. F. Bu, O. Gwon, G. Nam, H. Jang, S. Kim, Q. Zhong, J. Cho, G. Kim, *ACS Nano* **2017**, *11*, 11594.

[26] H. W. Liang, X. Zhuang, S. Brüller, X. Feng, K. Müllen, *Nat. Commun.* **2014**, *5*, 4973.

[27] a) Y. Zhao, K. Watanabe, K. Hashimoto, *J. Am. Chem. Soc.* **2012**, *134*, 19528; b) G. Nam, J. Park, S. T. Kim, D. B. Shin, N. J. Park, Y. Kim, J. S. Lee, J. Cho, *Nano Lett.* **2014**, *14*, 1870.

[28] a) Y. Zhao, R. Nakamura, K. Kamiya, S. Nakanishi, K. Hashimoto, *Nat. Commun.* **2013**, *4*, 2390; b) Z. X. Pei, H. F. Li, Y. Huang, Q. Xue, Y. Huang, M. S. Zhu, Z. F. Wang, C. Y. Zhi, *Energy Environ. Sci.* **2017**,*10*, 742. c) H. F. Wang, C. Tang, B. Wang, B. Q. Li, Q. Zhang, *Adv. Mater.* **2017**, *29*, 1702327.

[29] Y. Zan, Z. Zhang, H. Liu, M. Dou, F. Wang, *J. Mater. Chem. A* **2017**, *5*, 24329.

[30] Z. Liu, F. Sun, L. Gu, G. Chen, T. Shang, J. Liu, Z. Le, X. Li, H. B. Wu, Y. Lu, *Adv. Energy Mater.* **2017**, *7*, 1701154.

[31] S. Han, L. Hu, Z. Liang, S. Wageh, A. A. Al-Ghamdi, Y. Chen, X. Fang, *Adv. Funct. Mater.* **2015**, *24*, 5719.

[32] C. Y. Son, I. H. Kwak, Y. R. Lim, J. Park, *Chem. Commun.* **2016**, *52*, 2819.

[33] Y. Lu, Y. Jiang, X. Gao, X. Wang, W. Chen, *J. Am. Chem. Soc.* **2014**, *136*, 11687.

[34] M. Sun, H. Liu, Y. Liu, J. Qu, J. Li, *Nanoscale* **2015**, *7*, 1250.

[35] J. Chlistunoff, *J. Phys. Chem. C* **2011**, *115*, 6496.

[36] a) H. Teller, O. Krichevski, M. Gur, A. Gedanken, A. Schechter, *ACS Catal.* **2015**, *5*, 4260; b) Z. X. Pei, Z. J Tang, Z. X. Liu, Y. Huang, Y. K. Wang, H. F. Li, Q. Xue, M. S. Zhu, D. M. Tang, C. Y. Zhi, *J. Mater. Chem. A* **2018**, *6*, 489.

[37] a) M. Sun, D. Davenport, H. Liu, J. Qu, M. Elimelech, J. Li, *J. Mater. Chem. A* **2018**, *6*, 2527; b) L. T. Ma, S. M. Chen, Z. X. Pei, Y. Huang, G. J. Liang, F. Mo, Q. Yang, J. Su, Y. H. Gao, J. A. Zapien, C. Y. Zhi, *ACS Nano* **2018**, *12*, 1949.

